# Heterogeneous Interfaces of Magnetic CIP and Binary Dielectric Carbon-Based Material Toward High-Efficiency Microwave Attenuation

*Yongzhi Song[1], Song Bi[1]\*, Genliang Hou[1], Hao Li[1] and Zhaohui Liu[2]\**

[1]304 Department, Xi'an Research Institute of High-Tech, Xi'an, China, [2]College of Weapon Science and Technology, Xi'an Technological University, Xi'an, China

Carbon-based materials, as lightweight absorbers, have been widely applied in varied fields to counteract the adverse effects of electromagnetic waves. Nevertheless, there remain challenges in coping with the impairment of microwave absorption performance caused by the excessively high permittivity of carbon materials. Herein, carbonyl iron powder (CIP) was added to graphene oxide/carbon black (RGO-CB) composites to adjust the permittivity improving impedance matching and electromagnetic absorption properties. In this work, the RGO provides a three-dimensional structure net, which introduces circularly and variously electromagnetic loss interfaces within the RGO-CB/CIP composites. Owing to the unique architecture and synergy of the three components, the as-prepared absorber exhibits good impedance matching and gratifying microwave absorption properties. It was found that the 1:1 mixture of RGO-CB and CIP in the composite had superb impedance matching at the thicknesses of 2.6 and 2.7 mm to achieve complete X-band microwave absorption. Such excellent performance benefits from the multiple polarization provided by the heterogeneous interfaces and the ideal impedance match attributed to the tunable permeability and permittivity of this work.

**Keywords: RGO, CIP, CB, X-band, microwave absorption, reflection loss**

## INTRODUCTION

Up to now, the range of X-band of electromagnetic waves is still the most critical frequency of electromagnetic waves in civil and military aerospace and space technology (Micheli et al., 2010; Vinayasree et al., 2013; Silva and Rezende, 2021). Though with increasing convenience to human life, the ensuing electromagnetic pollution can greatly impact human health and sophisticated electronic devices. Thus, microwave absorbing materials have drawn the attention of researchers worldwide. A microwave absorbing material with lightweight, strong absorption, small thickness, and wide absorption bandwidth is considered ideal for attenuating electromagnetic energies (He et al., 2020; Liang et al., 2020; Wang et al., 2020).

As one of the essential absorbing properties, impedance matching determines whether electromagnetic waves can enter from free space into the absorber, which is an essential factor that must be considered when designing an absorber. The current single absorbing materials, including magnetic and electric loss absorbing material, can not achieve good impedance matching

conditions due to the large gap between complex permittivity and permeability (Li et al., 2018). Apart from that, the attenuation constant is another factor that must be considered for designing a microwave absorbing material. When electromagnetic waves pass through the surface of the absorber and enter the interior, it is vital that incident waves can be attenuated rapidly to achieve effective absorption (Li et al., 2022). The perfect combination of attenuation constants and impedance matching will be a top priority for scholars designing ideal absorbers (Shen et al., 2021).

Typical nanostructured carbon, including graphite, CB and carbon nanotubes (CNTs) materials, are usually applied as microwave absorber given their excellent dielectric properties, low density and other unique physical and chemical properties (Li et al., 2018). In recent years, graphene, as a new type of nanostructured carbon material, has become a focus of attention for its excellent electrical, thermal, mechanical properties and high specific surface area (Song et al., 2021). Pure graphene absorbers mainly rely on conduction losses to attenuate electromagnetic wave energies (Zhang et al., 2019). However, good electrical conductivity hampers impedance matching, leading to the inability of electromagnetic waves to cross the surface of the absorber. This means that the best way to take advantage of graphene's superb dielectric loss is to improve impedance matching. As another member of the carbon family, carbon black possesses both excellent dielectric properties and low density. One of the benefits of using carbon black as a filler between graphene sheets is that it preserves graphene's dielectric properties while also reducing its conductivity, thus improving the wave absorption properties of graphene.

As of now, the most widely studied magnetic microwave-absorbing materials include $Fe_3O_4$, cobalt-zinc ferrite, magnetite nanoparticles, Ni, and carbonyl iron powders (CIP) (He et al., 2017; Li et al., 2017; Liao et al., 2018; Xu et al., 2018; Wang et al., 2019; Wang et al., 2020; Reyes-Ortega et al., 2021; Wang et al., 2021). Carbonyl iron powders (CIP) are commonly used in composites because of their high saturation magnetization strength, low coercivity, and good magnetic properties (Sista et al., 2021). However, the high density and filling ratio of CIP prevent it from being widely used. In general, it is hard to achieve the desired electromagnetic wave absorption properties solely by filling absorbers with dielectric or magnetic media. Thus, researchers attempt to combine magnetic and carbon materials in composite or use hybridized approaches to improve the impedance matching as well as its microwave loss performance (Yang et al., 2020; Han et al., 2021; Jang et al., 2021). Recently, Liu et al. (Liu et al., 2010) investigated the microwave absorption performance of monolayer coatings consisting of CIP and CB in the range of 2–18 GHz. They found that at a sample thickness of 1.5 mm, the absorption bandwidth broadened with increasing CB content, especially when the ratio of CIP and CB was 25 wt.% respectively, and the absorption bandwidth (RL < −4 dB) reached 10.1 GHz (7.9–18 GHz). Lopes et al. (Lopes et al., 2020) prepared hybrid composites with 30 wt.% MnZn ferrites, 50 wt.% CIP and 1 wt.% CNTs and investigated their electromagnetic absorption properties on silicone rubber in the X-band (8.2–12.4 GHz).

The $RL_{max}$ was found at 2.3 mm thickness, with a value of −21 dB. Xu et al. (Xu et al., 2015)evaluated the microwave absorption performance of the graphene doped with CIP and found that the CIP/GO composites filled with 5 vol% had excellent wave absorption performance at 2–18 GHz, with the $RL_{max}$ of - 25.14 dB at 6 mm and -26.52 dB at 8 mm. The above studies showed that many scholars have tried to combine the properties of CIP and carbon-based materials to prepare an ideal microwave absorbing material and have indeed achieved some progress. However, there still exist deficiencies such as the lack of absorbing bandwidth, the low absorbing intensity, and the excessive thickness.

In order to overcome these deficiencies, the present RGO-CB/CIP composite was synthesized *via* a three-step method. GO was prepared based on the Hummers method in the first step and followed by the one-pot method to attach the CB with RGO during the reduction of GO to GRO. Finally, the group on RGO-CB was activated by acidification treatment while roughening the CIP surface to facilitate the binding of CIP to RGO-CB. This work concentrates on the electromagnetic and microwave absorption properties of RGO-CB/CIP composites in 8–12.4 GHz. The effects of CIP loading and absorber thickness on the microwave absorption properties of the composites were discussed, and the microwave absorption mechanism was analyzed in depth.
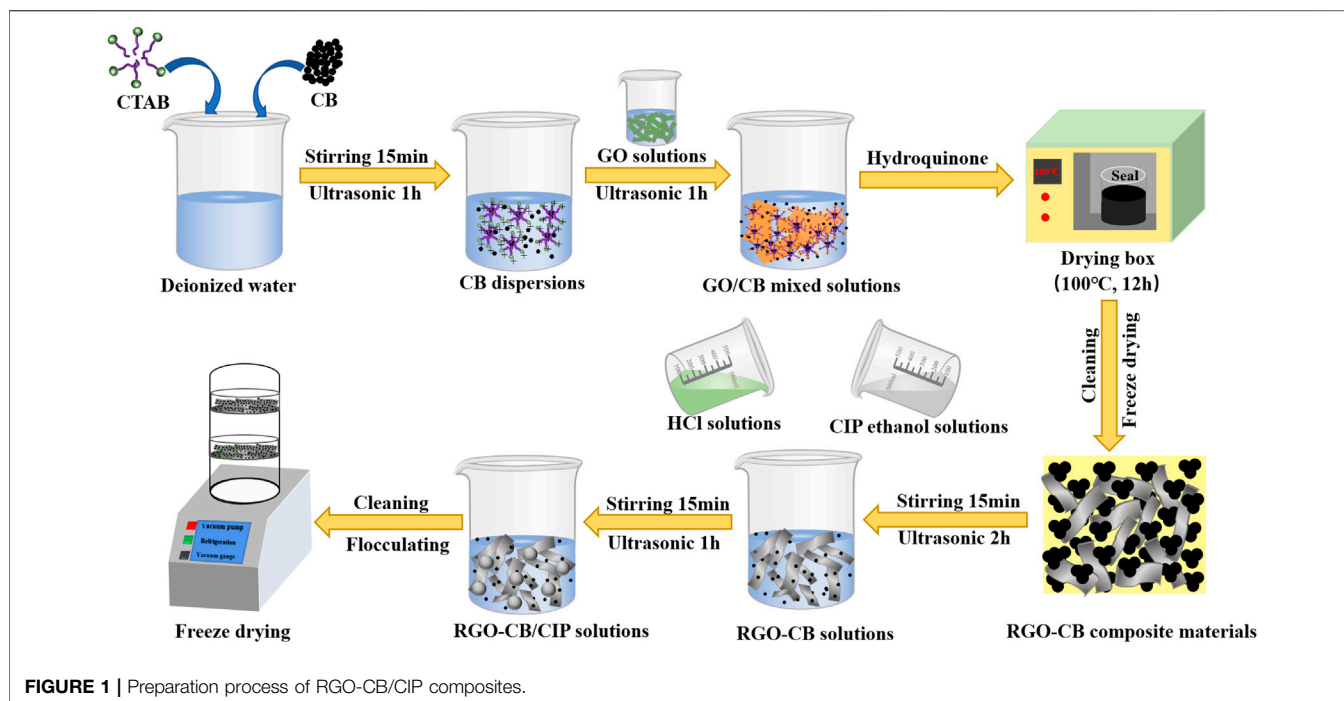
## EXPERIMENTS

### Preparation of Aqueous GO Solutions

Based on the modified Hummers method, graphene oxide solutions were prepared. Graphite powder (6 g) and $NaNO_3$ were added to concentrated $H_2SO_4$ (360 ml) stirred under an ice water bath for 1 h, and then 18 g of $KMnO_4$ powder was added slowly. A slow addition rate and a temperature of lower than 5°C were stressed to the safety of this method. After 2 h of stirring, the mixture turned to dark green-black colour. The solution was then heated to 30°C and stirred for another 2 h. Deionized water (600 ml) was added to the solution and stirred for 0.5 h $H_2O_2$ (150 ml 5%) was then added and stirred for 0.5 h. After 12 h of settling, the solution was poured off its top layer, and the precipitate was washed with hydrochloric acid solution and deionized water. After six times centrifugation and washed in total, the pure precipitate was obtained. In the end, 500 ml GO solution (GOs) was prepared by dissolving the precipitate in deionized water and stirring. The schematic is shown in **Figure 1**.

### Preparation of RGO-CB Composites

RGO-CB was prepared by the one-pot method. Firstly, 500 ml of deionized water was mixed with 2.4 g of CB powder and 1.2 g of CTAB (hexadecyl trimethyl ammonium bromide), and the mixture was stirred for 15 min before being sonicated for 1 h. At the same time, 100 ml of GOs was taken and sonicated for 1 h. Once the CB dispersion solution was sonicated, GOs was added and sonicated for an additional hour. After the correct amount of p-diphenol was added, the beaker was sealed with cling film. The obtained mixed solution was transferred to a drying oven and

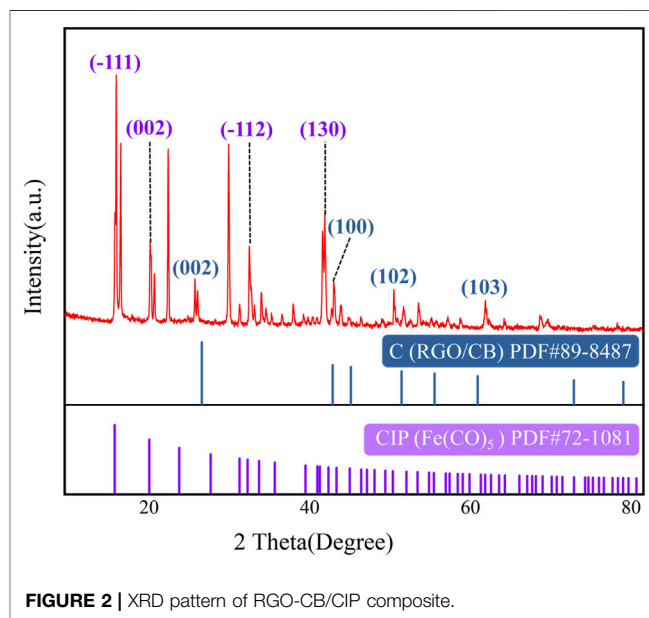**FIGURE 1 |** Preparation process of RGO-CB/CIP composites.

heated at 100°C for 12 h, and then the precipitate was washed with deionized water and cycled twice. After vacuum freeze-drying treatment, CB/RGO composites were obtained.

## Preparation of RGO-CB/CIP Composites

RGO-CB/CIP composite was synthesized by a simple acidification process. The CB/RGO solution was generated by dispersing 1.2 g of CB/RGO powder in 100 ml of deionized water and sonicating for 2 h. To get a well-mixed solution, 200 ml of HCl (35%) was added to the CB/RGO solution and constantly stirred at room temperature. An appropriate amount of CIP was then added to 100 ml of ethanol and stirred vigorously to form a homogeneous dispersion before being added to the CB/RGO solution at room temperature. To flocculate, the mixture was sonicated for 1 h and then held. Finally, the flocs were removed by filtration, washed several times with deionized water and ethanol, and dried in a vacuum oven at 70°C for 12 h. Four sample materials were made according to the proportion of CIP and CB/RGO (1:2, 1:1, 2:1, 3:1, S1, S2, S3 and S4, respectively).

## Characterization

These composites were characterized using a variety of methods. The microstructure and morphology of the samples were observed by a ZEISS GeminiSEM 300 scanning electron microscope (SEM) and an F200X transmission electron microscope (TEM) from Germany. Coaxial line measurements of electromagnetic parameters were performed with a KEYSIGHT E5071C vector network analyzer. The specimens were prepared by homogeneously mixing paraffin wax with the sample at a mass ratio of 3:7 and then pressing the mixture into an annular ring with an external diameter of 7.00 mm and an internal diameter of 3.04 mm.



**FIGURE 2 |** XRD pattern of RGO-CB/CIP composite.

## RESULTS AND DISCUSSION

RGO-CB/CIP composite's XRD pattern was depicted in **Figure 2**. It showed the presence of four phases of carbon in the RGO-CB/CIP composite by comparing the test data with the PDF#89-8487 standard card, with $2\theta$ values equal to 26.55°, 42.37°, 50.71°, and 59.91°, which can be attributed to (002), (100), (102) and (103) crystal planes of RGO or CB, respectively. Compared with the standard card PDF#72-1081, there were majorly four CIP crystal planes in the RGO-CB/CIP composite,
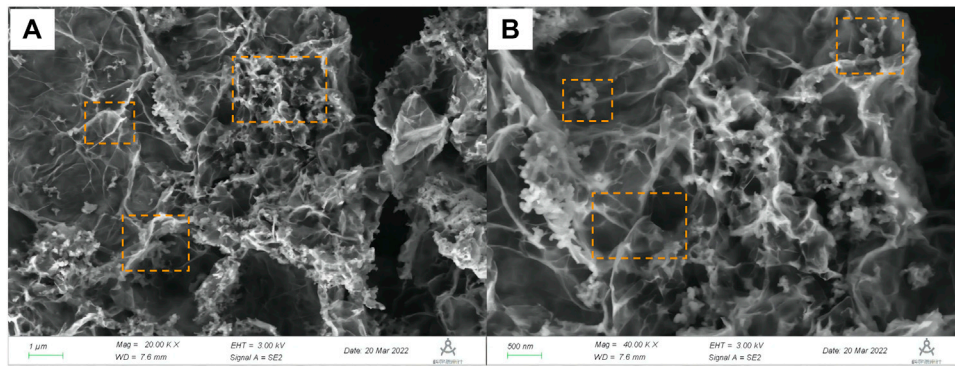
**FIGURE 3** | SEM image of the RGO-CB/CIP composite. **(A)** The interface formed by the folding of RGO itself; **(B)** CIP and CB are attached to the RGO surface to form a heterogeneous interface.
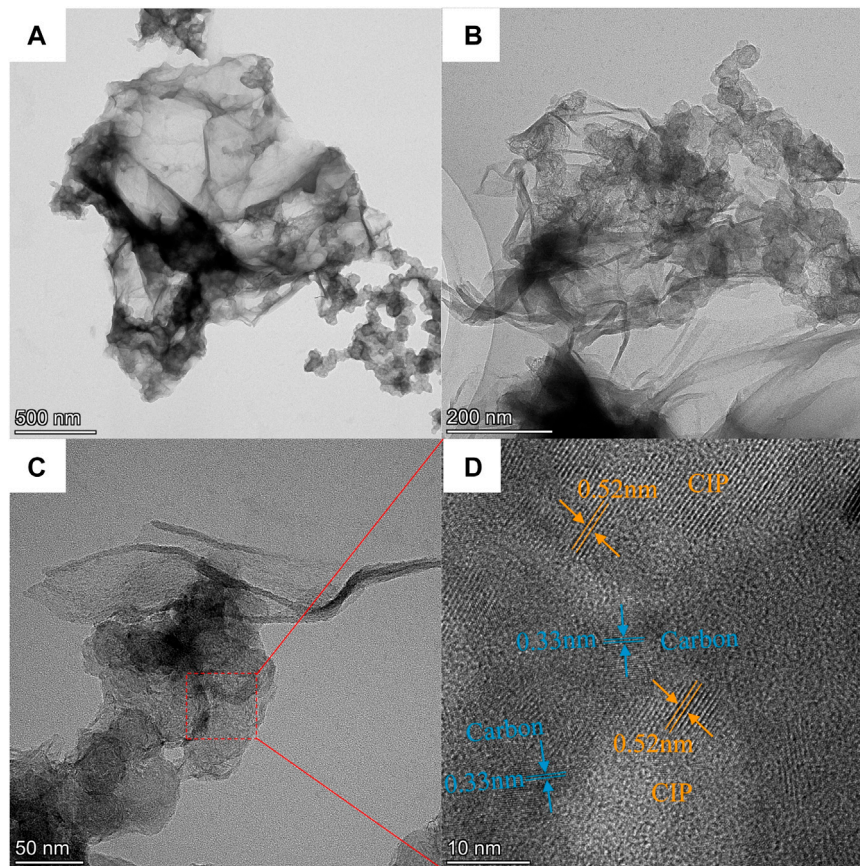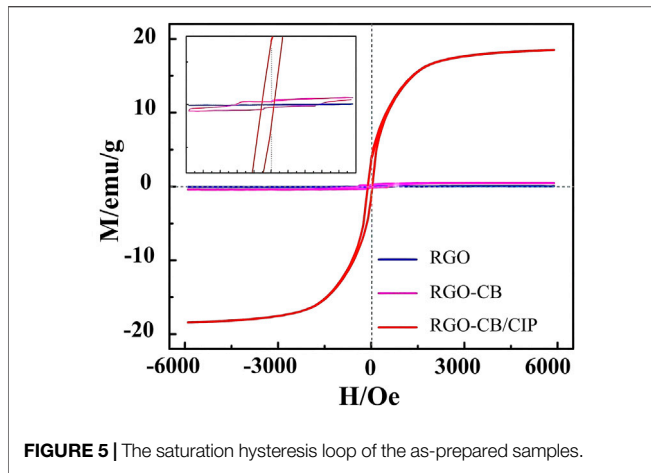


**FIGURE 4** | Transmission electron micrograph of RGO-CB/CIP composite. **(A,B)** CB and CIP particles wrapped with RGO film; **(C)** interface between CB and CIP; **(D)** high resolution TEM image of the selected part of **(C)**, showing lattice fringe spacing of CIP and CB.

(−111), (002), (−112) and (130), corresponding to the 2θ values of 16.88°, 20.06°, 23.26°, and 40.57°, respectively. The characteristic diffraction peaks show that the CIP successfully grew in the composite.

**Figure 3** shows the RGO-CB/CIP composite's SEM image. Obviously, there are abundant crumples on the surface of RGO, and multiple heterogeneous interfaces are formed through the contact between individual folds or the connection of CB and

FIGURE 5 | The saturation hysteresis loop of the as-prepared samples.

nanospheres were tightly adhered to the RGO surface, especially between the individual folds. Therefore, the two-dimensional graphene nanosheets are developed into three-dimensional structural composite materials.

**Figure 4** shows the morphology of the RGO-CB/CIP composite taken by the transmission electron microscope. From **Figures 4A,B**, it can be intuitively observed that the soft RGO film is like a giant net covering CB and CIP, forming a cladding structure. This structure would easily lead to the confinement effect (Hao et al., 2016) and could significantly improve the electromagnetic wave attenuation capability of the RGO-CB/CIP composite. By performing a high-resolution TEM (**Figure 4D**) of the interface shown in **Figure 4C**, it can be confirmed that CIP and CB were tangled with each other by the lattice fringe spacing of ~0.52 and ~0.33 nm corresponding to the d-spacing of CIP(−111) and carbon (002), respectively. It provides visual structural evidence for the existence of interface polarization to attenuate microwaves in the composite.

The as-prepared samples were applied to the test of magnetic properties at room temperature and the magnetic field was 6,000 Oe. The hysteresis loops of the samples are shown in **Figure 5**. It is evident that the growth of CB has limited influence on the magnetic properties of RGO, while the
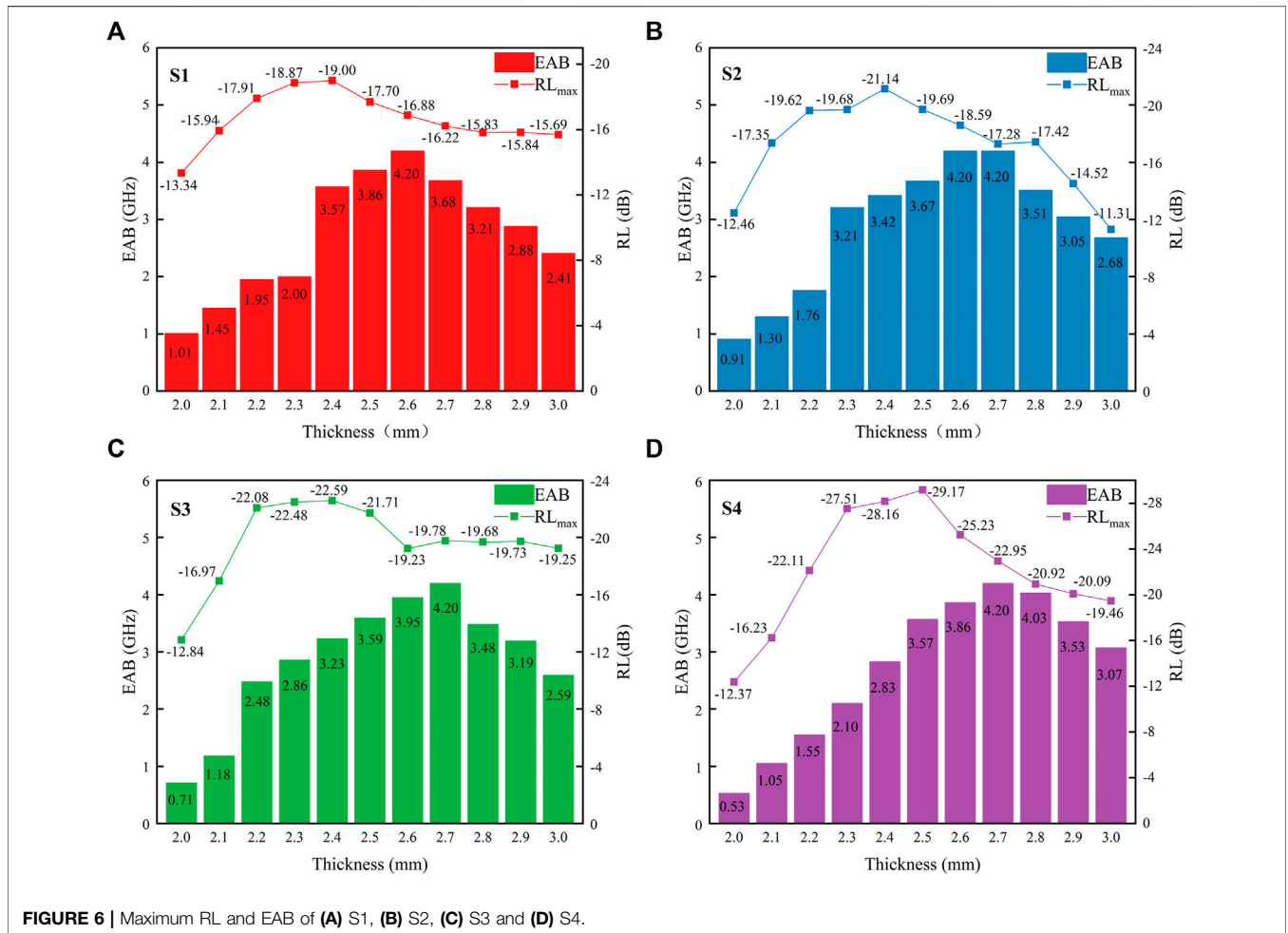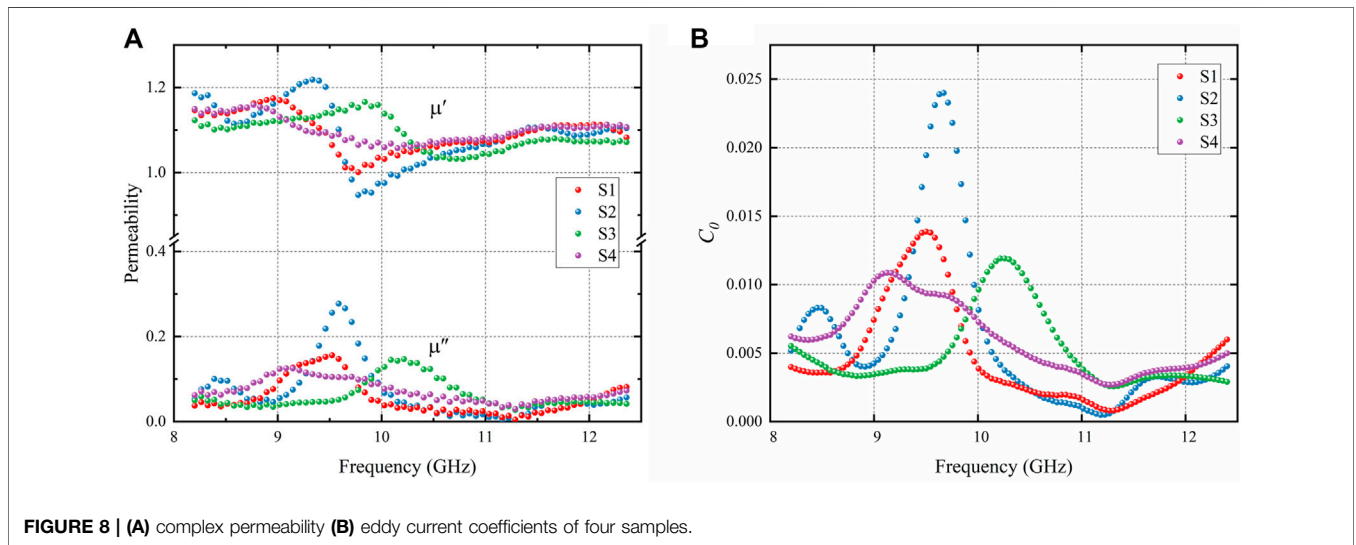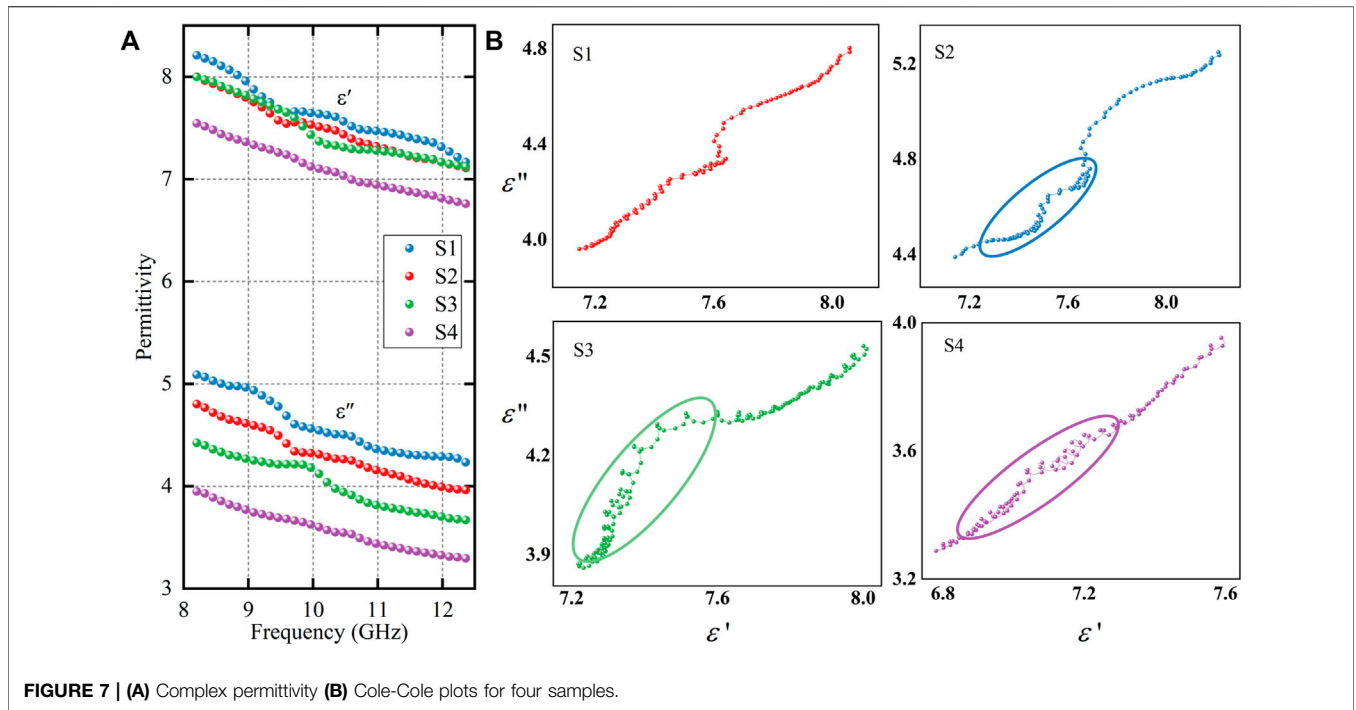
CIP, which would lead to multiple interface polarization. Meanwhile, CB, CIP and RGO were superimposed in sequence, forming a multi-stage structure. The interface polarization and multiple scattering characteristics of the multi-stage structure might effectively improve the absorbing properties (Weng et al., 2022). It was evident that the



FIGURE 6 | Maximum RL and EAB of **(A)** S1, **(B)** S2, **(C)** S3 and **(D)** S4.

FIGURE 7 | (A) Complex permittivity (B) Cole-Cole plots for four samples.



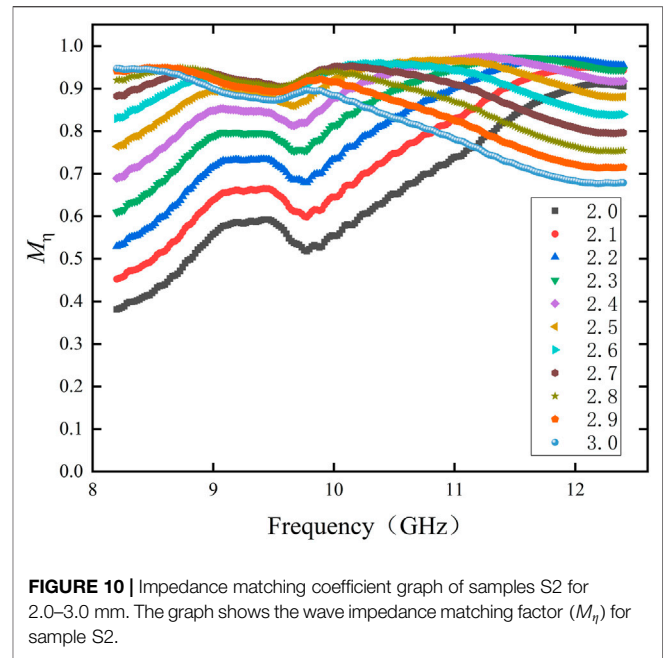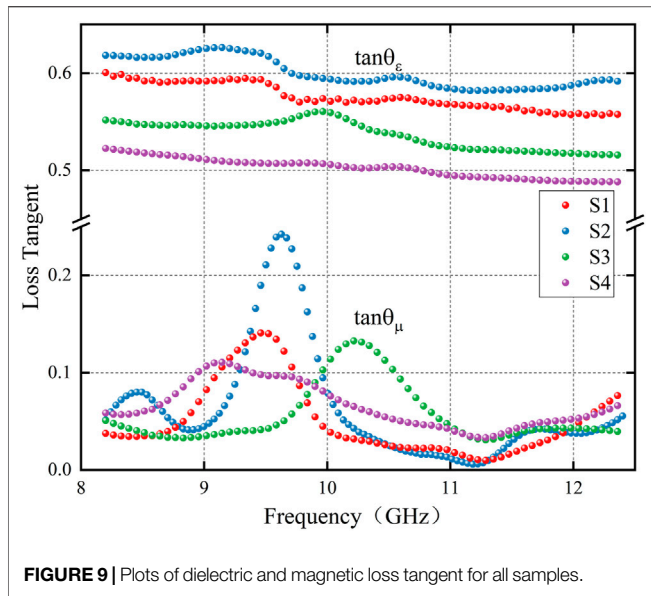FIGURE 8 | (A) complex permeability (B) eddy current coefficients of four samples.

saturation magnetization of the RGO-CB/CIP is much higher than that of RGO and RGO-CB samples since the CIP is a typical magnetic material, which shows that the CIP is successfully growing with the RGO-CB.

RL (reflection loss) was calculated from the relative complex permittivity ($\varepsilon_r$) and relative complex permeability ($\mu_r$) measured by the vector network analyzer. According to transmission line theory, RL can be calculated by.

$$\text{RL(dB)} = 20\lg\left|\frac{Z_{in}-1}{Z_{in}+1}\right| \qquad (1)$$

$$Z_{in} = \sqrt{\frac{\mu_r}{\varepsilon_r}}\tanh\left[j\left(\frac{2f\pi}{c}d\right)\sqrt{\mu_r + \varepsilon_r}\right] \qquad (2)$$

Where $Z_{in}$ is the normalized input impedance, and d is the thickness of the material. Effective microwave absorption is defined as less than 10% reflectance, i.e., RL < −10 dB, and the corresponding frequency range is the effective absorption bandwidth (EAB). Absorption and reflection losses are shown in **Figure 6** for the various thicknesses of samples, and all samples have good microwave absorption in X-band. Based on transmission line theory and calculated S1's

FIGURE 9 | Plots of dielectric and magnetic loss tangent for all samples.



FIGURE 10 | Impedance matching coefficient graph of samples S2 for 2.0–3.0 mm. The graph shows the wave impedance matching factor ($M_\eta$) for sample S2.

electromagnetic parameters, it is found that the EAB of S1 is equal to 4.2 GHz, which covers the X-band (8.2–12.4 GHz) with a maximum of RL$_{max}$ of −16.88 dB at 2.6 mm (**Figure 6A**). The RL$_{max}$ of −18.59 dB and −17.28 dB are achieved by S2 at 2.6 and 2.7 mm thicknesses, respectively, with full EAB coverage of the X-band (**Figure 6B**). RL$_{max}$ of −19.78 dB and -20.92 dB for S3 and S4 were achieved (**Figures 6C,D**). Meanwhile, the EAB of both S3 and S4 covered the X-band at 2.7 mm. Aside from this, it is clear from the graph that the increase of CIP content is positively associated with the maximum intensity of RLmax for the four samples in the 2.0–3.0 mm range, with RLmax values of −19.00 dB, −21.14 dB, −22.59 dB, and −29.17 dB, corresponding the thickness of 2.4 mm (S1), 2.4 mm (S2), 2.4 mm (S3) and 2.5 mm (S4,) respectively.

The absorption properties of electromagnetic waves are closely related to the complex permittivity and complex permeability. In general, the real part of the complex permittivity ($\varepsilon_r = \varepsilon' - i\varepsilon''$) and the real part of the complex permeability ($\mu_r = \mu' - j\mu''$) represents the material's ability to store electrical and magnetic energy, respectively. In contrast, the imaginary part of the complex permittivity ($\varepsilon''$) and the imaginary part ($\mu''$) of the complex permeability represents the ability of the material to attenuate electrical energy and magnetic energy, respectively. According to **Figure 7A**, the real ($\varepsilon'$) and imaginary ($\varepsilon''$) parts of the dielectric constant decrease with increasing frequency, which is typical of dispersive behaviour and exacerbates polarization hysteresis at high frequencies. **Figure 7A** shows that the highest values of S2 are followed by S1, S3, and S4 in ascending order. Moreover, as CIP content increases, permittivity falls steadily apart from an exception for S2, which may result from moderate conduction loss and polarization loss.

Based on the conductive network manner proposed by Cao and his coworker, the electron hopping between CB-RGO layers significantly affects the conductivity of the composite

(Wang et al., 2018). When introduced, CIP exhibits resistive properties that hinder inter-layer electron hopping and intra-layer electron migration, reducing conductive network connections and lowering the conductivity of the composites.

According to the Debye theory, the $\varepsilon'$ and $\varepsilon''$ of the dielectric constants can be described as follows.
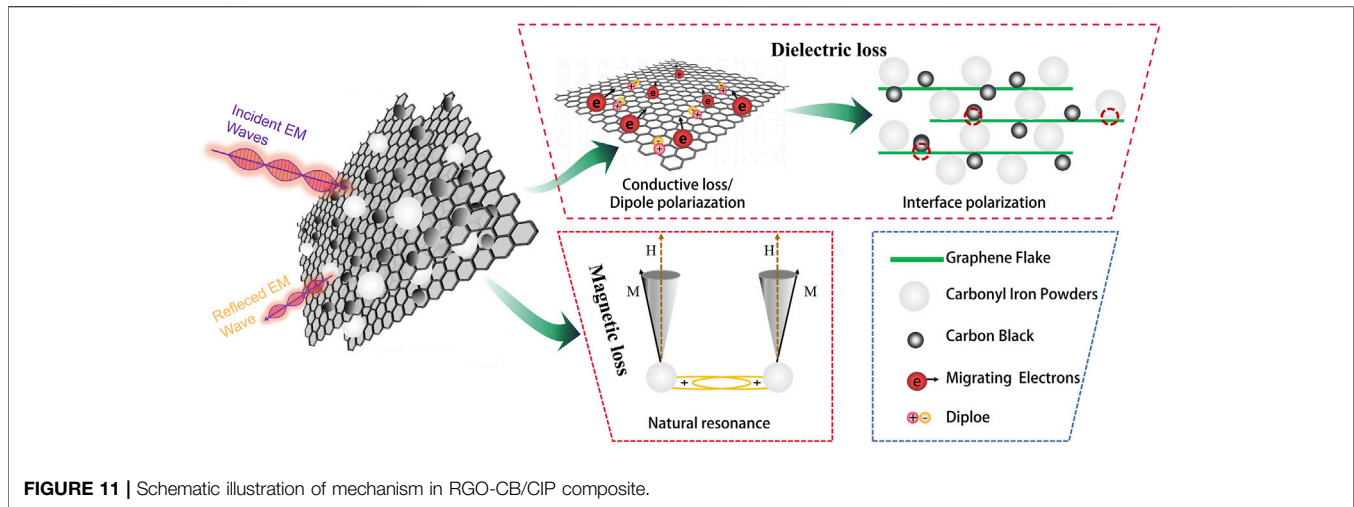
$$\varepsilon' = \varepsilon_\infty + \frac{\varepsilon_s - \varepsilon_\infty}{1 + \omega^2\tau^2} \tag{3}$$

$$\varepsilon'' = \frac{\varepsilon_s - \varepsilon_\infty}{1 + \omega^2\tau^2}\omega\tau + \frac{\sigma}{\omega\varepsilon_0} \tag{4}$$

Based on the two equations above, the relationship between $\varepsilon'$ and $\varepsilon''$ can be calculated as

$$\left(\varepsilon' - \frac{\varepsilon_s + \varepsilon_\infty}{2}\right)^2 + \left(\varepsilon''\right)^2 = \left(\frac{\varepsilon_s - \varepsilon_\infty}{2}\right)^2 \tag{5}$$

In the above equations, $\omega = 2\pi f$ and $f$ is the frequency. Where $\tau$, $\varepsilon_\infty$ and $\varepsilon_s$ are the relaxation time, the permittivity at an infinite frequency and the static dielectric constant, respectively. The relationship graph between $\varepsilon'$ and $\varepsilon''$ was shown in **Figure 7B**, and there are a considerable number of semicircles (denoted as Cole-Cole semicircle), which indicates the corresponding Debye relaxation process (Deng et al., 2020). In addition to the dipole polarization caused by graphene defects and functional groups, from the four samples in this paper, it can be observed that S1 does not have a distinct Debay ring. With the increase in the amount of CIP, S2 shows a few semicircles, S3 has the highest number of semicircles, and the number of semicircles in S4 decreases when the proportion of CIP and CB/RGO reaches 3:1. It can be speculated that the addition of CIP forms a interface between RGO-CB, leading to the aggregation and inhomogeneous distribution of charges at the interface between RGO-CB/

**FIGURE 11 |** Schematic illustration of mechanism in RGO-CB/CIP composite.

CIP, which generates macroscopic electric moments. Under the precondition of ensuring the dielectric properties of RGO-CB, increasing the amount of CIP can form more interface, resulting in more charge accumulation at the interface and enhanced interfacial polarization within the material. Furthermore, a visible peak appears in the curve of S3 at 10 GHz, which indicates the most robust interfacial polarization in S3. Conversely, as can be seen from S4, a further increase in the CIP content diminishes the electrical conductivity of the composite, resulting in weaker interfacial polarization.

As can be seen in **Figure 8A**, the mean values of $\mu'$ and $\mu''$ for all samples generally appear to increase with the amount of CIP and show clear resonance peaks, indicating that the CIP causes magnetic resonance. Sample S2 has the highest resonance peak, which means that the magnetic loss is the strongest. The manners of magnetic loss generally include hysteresis loss, domain wall resonance, natural resonance, and eddy current loss. In the frequency range of 8–12.4 GHz, the ways of magnetic loss are mainly natural resonance and eddy current loss (Zhao et al., 2019). According to the principle of eddy current loss, the value $C_0 = \mu''(\mu')^{-2}f^{-1}$ would remain constant with frequency (Zhou et al., 2019). The value $C_0$ of the four samples, as shown in the **Figure 8B**, fluctuates within the 8–12.4 GHz frequency, indicating that the electromagnetic magnetic loss manner of the RGO-CB/CIP composite in this X-band does not contain eddy current loss or is not strong enough. It can be inferred from above that the primary manner of magnetic loss for RGO-CB/CIP composite is natural resonance.

**Figure 9** shows the dielectric loss tangent and the magnetic loss tangent of the RGO-CB/CIP composite from 8 to 12.4 GHz. The dielectric loss tangent is much larger than the magnetic loss tangent, indicating that the dielectric loss is dominant among the two loss manners. As CIP is a kind of magnetically lossy absorbing material, the average value of the magnetic loss tangent increases gradually as the CIP content. However, something is unexpected that the content of CIP increasing makes the dielectric loss tangent of S2 larger than that of S1.

These results suggested that adding an appropriate amount of CIP could increase the number of heterogeneous interfaces in the composite, enhancing the interfacial polarization of the composite and improving its dielectric loss strength. However, with the continuing increase of CIP, the dielectric loss tangent value of S3 decreases abruptly and reaches its lowest value at S4. This result also corroborates the previous finding of the decrease in S3 and S4 Debay rings. In short, the excessive addition of CIP weakens the connection points between graphene layers, and widens their distance, leading to the difficulty of electron hopping between the layers, thus hindering the interfacial polarization. As the CIP is in a resistive state on graphene, excessive concentration also inevitably leads to a less efficient conductive network and makes it difficult for conductive losses to complete for electromagnetic waves attenuation.

$$M_\eta = \frac{2 \times \mathrm{Re}\left[\sqrt{\frac{\mu_r}{\varepsilon_r}}\right]}{\left|\sqrt{\frac{\mu_r}{\varepsilon_r}}\right|^2 + 1} \qquad (6)$$

Where Re [X] is taken as the real part of the complex number X, $\varepsilon_r$ denotes the relative complex permittivity and $\mu_r$ is the relative complex permeability. The ideal impedance matching condition is that the relative wave impedance of the medium is equal to the relative wave impedance of the air, so the closer the wave impedance matching coefficient ($M_\eta$) is to 1, the better the electromagnetic impedance matching of the material. It can be seen from the graph (**Figure 10**) that there was a tendency for the wave impedance matching coefficient to increase and then decrease for all thicknesses, especially for the samples of thickness from 2.5 to 2.8 mm, which all had values equal to 1 at a specific frequency range before decreasing with increasing frequency. As the thickness increases, the specific frequency range, at which the $M_\eta$ value of S2 reaches 1, shifts continuously to the left. Comparing $M_\eta$ at the thicknesses from 2.0 to 3.0 mm, it can be found that only when thicknesses are between 2.6 and 2.7 mm, can every point's values reach 0.8 or more. That can

explain why the absorption bandwidth of each sample tended to increase and then decrease as the thickness increased, with only the thicknesses of 2.6–2.7 mm meeting the entire frequency range of 8.0–12.4 GHz.

RGO-CB/CIP composite absorption of electromagnetic waves was summarized in **Figure 11**. Impedance matching was critical to ensure the vast majority of electromagnetic waves penetrate the composite's interior through the air. The energy of the incident electromagnetic waves was then converted into heat dissipation inside the absorber by various absorption mechanisms, as elaborated below.

1 Conductive losses. In the composite material, graphene, carbon black and CIP formed a three-dimension conductive network of limited resistance. When electromagnetic waves passed through the composite material, induced currents were formed within the material and converted to thermal energy as the induced currents passed through the resistive conductive network.

2 Polarization loss. As a ternary composite, the RGO-CB/CIP composite had multiple forms of phase boundaries. The different phase boundaries in RGO-CB/CIP can accumulate charge and lead to interfacial polarization. Also, in reduced graphene oxide, there is a large number of functional groups and defects, which can act as dipole centres under the influence of a magnetic field and cause dipole polarization.

3 Magnetic losses. Due to the presence of CIP in the RGO-CB/CIP complex, the RGO-CB/CIP complex is subjected to not only dielectric losses but also magnetic losses. The leading cause of magnetic loss was natural resonance.

## CONCLUSION

In summary, RGO-CB/CIP composite was prepared by hummers method, one-pot method, and acidified mixing method. GO was grafted with CB during the reduction process of GO to RGO, forming an RGO-CB composite, which would be tightly CIP-coated. By combining the magnetic loss material with the dielectric loss material, the RGO-CB/CIP composite achieved better impedance matching performance. Most of the electromagnetic waves of the X-band can enter the material. The redox process of graphene led to the formation of many defects on the surface of graphene, which became active centres for dipole polarization. In addition, the heterogeneous interface formed between RGO, CB, and CIP provided conditions for the accumulation of charges, and the multi-heterogeneous interface dramatically enhanced the interface polarization. The results demonstrated that the sample, whose proportion of CIP and RGO-CB is 1:1, had an absorption bandwidth covering the X-band at 2.6 and 2.7 mm, and had microwave absorption peaks at −18.59 dB and -17.28 dB, respectively. This research provided a method for making X-band-targeted absorbing materials, as well as an in-depth analysis of the absorption mechanism, in the hopes of serving as a guide for future researchers.

## DATA AVAILABILITY STATEMENT

The raw data supporting the conclusion of this article will be made available by the authors, without undue reservation.

## AUTHOR CONTRIBUTIONS

The thesis was completed by YS under the supervision of SB and GH for the experiments and thesis writing. The protocol design of the experiments was done by HL, and ZL was responsible for the theoretical study and image processing.

## FUNDING

## REFERENCES

Deng, B., Xiang, Z., Xiong, J., Liu, Z., Yu, L., and Lu, W. (2020). Sandwich-like Fe&TiO2@C Nanocomposites Derived from MXene/Fe-MOFs Hybrids for Electromagnetic Absorption. *Nano-Micro Lett.* 12, 1–16. doi:10.1007/s40820-020-0398-2

Han, C., Zhang, M., Cao, W.-Q., and Cao, M.-S. (2021). Electrospinning and *In-Situ* Hierarchical Thermal Treatment to Tailor C-NiCo2O4 Nanofibers for Tunable Microwave Absorption. *Carbon* 171, 953–962. doi:10.1016/j.carbon.2020.09.067

Hao, X.-Q., Yang, H., Jin, Z.-L., Xu, J., Min, S.-X., and Lü, G.-X. (2016). Quantum Confinement Effect of Graphene-like C3N4 Nanosheets for Efficient Photocatalytic Hydrogen Production fromWater Splitting. *Acta Physico-Chimica Sin.* 32, 2581–2592. doi:10.3866/PKU.WHXB201606226

He, G., Duan, Y., and Pang, H. (2020). Microwave Absorption of Crystalline Fe/MnO@C Nanocapsules Embedded in Amorphous Carbon. *Nano-Micro Lett.* 12, 1–16. doi:10.1007/s40820-020-0388-4

He, P., Hou, Z.-L., Zhang, K.-L., Li, J., Yin, K., Feng, S., et al. (2017). Lightweight Ferroferric Oxide Nanotubes with Natural Resonance Property and Design for Broadband Microwave Absorption. *J. Mater Sci.* 52, 8258–8267. doi:10.1007/s10853-017-1041-6

Jang, W., Mallesh, S., Gu, M., and Kim, K. H. (2021). Edge Selectively Oxidized Graphene on Carbonyl Iron Composites for Microwave Absorption and Radar Cross-Section Performance at X- and Ku-Band. *J. Alloys Compd.* 886, 161230. doi:10.1016/j.jallcom.2021.161230

Li, J., Bi, S., Mei, B., Shi, F., Cheng, W., Su, X., et al. (2017). Effects of Three-Dimensional Reduced Graphene Oxide Coupled with Nickel Nanoparticles on the Microwave Absorption of Carbon Fiber-Based Composites. *J. Alloys Compd.* 717, 205–213. doi:10.1016/j.jallcom.2017.03.098

Li, Y., Sun, N., Liu, J., Hao, X., Du, J., Yang, H., et al. (2018). Multifunctional BiFeO3 Composites: Absorption Attenuation Dominated Effective Electromagnetic Interference Shielding and Electromagnetic Absorption Induced by Multiple Dielectric and Magnetic Relaxations. *Compos. Sci. Technol.* 159, 240–250. doi:10.1016/j.compscitech.2018.02.014

Li, Y., Wang, G., Gong, A., Zhang, S., Liu, J., Sun, N., et al. (2022). High-Performance Ferroelectric Electromagnetic Attenuation Materials with Multiple Polar Units Based on Nanodomain Engineering. *Small (Weinheim der Bergstrasse, Ger.* 18, e2106302–n/a. doi:10.1002/smll.202106302

Liang, X., Man, Z., Quan, B., Zheng, J., Gu, W., Zhang, Z., et al. (2020). Environment-Stable CoxNiy Encapsulation in Stacked Porous Carbon Nanosheets for Enhanced Microwave Absorption. *Nano-Micro Lett.* 12, 1–12. doi:10.1007/s40820-020-00432-2

Liao, Q., He, M., Zhou, Y., Nie, S., Wang, Y., Hu, S., et al. (2018). Highly Cuboid-Shaped Heterobimetallic Metal-Organic Frameworks Derived from Porous Co/ZnO/C Microrods with Improved Electromagnetic Wave Absorption Capabilities. *ACS Appl. Mat. Interfaces* 10, 29136–29144. doi:10.1021/acsami.8b09093

Liu, L., Duan, Y., Ma, L., Liu, S., and Yu, Z. (2010). Microwave Absorption Properties of a Wave-Absorbing Coating Employing Carbonyl-Iron Powder and Carbon Black. *Appl. Surf. Sci.* 257, 842–846. doi:10.1016/j.apsusc.2010.07.078

Lopes, B. H. K., Portes, R. C., Amaral Junior, M. A. D., Florez-Vergara, D. E., Gama, A. M., Silva, V. A., et al. (2020). X Band Electromagnetic Property Influence of Multi-Walled Carbon Nanotube in Hybrid MnZn Ferrite and Carbonyl Iron Composites. *J. Mater. Res. Technol.* 9, 2369–2375. doi:10.1016/j.jmrt.2019.12.068

Micheli, D., Apollo, C., Pastore, R., and Marchetti, M. (2010). X-band Microwave Characterization of Carbon-Based Nanocomposite Material, Absorption Capability Comparison and RAS Design Simulation. *Compos. Sci. Technol.* 70, 400–409. doi:10.1016/j.compscitech.2009.11.015

Reyes-Ortega, F., Delgado, Á., and Iglesias, G. (2021). Modulation of the Magnetic Hyperthermia Response Using Different Superparamagnetic Iron Oxide Nanoparticle Morphologies. *Nanomaterials* 11, 627. doi:10.3390/nano11030627

Shen, J., Zhang, D., Han, C., Wang, Y., Zeng, G., and Zhang, H. (2021). Three-dimensional Flower-like FeCoNi/reduced Graphene Oxide Nanosheets with Enhanced Impedance Matching for High-Performance Electromagnetic Wave Absorption. *J. Alloys Compd.* 883, 160877. doi:10.1016/j.jallcom.2021.160877

Silva, V. A., and Rezende, M. C. (2021). S-parameters, Electrical Permittivity, and Absorbing Energy Measurements of Carbon Nanotubes-based Composites in X-band. *J. Appl. Polym. Sci.* 138, 49843–n/a. doi:10.1002/app.49843

Sista, K. S., Dwarapudi, S., Kumar, D., Sinha, G. R., and Moon, A. P. (2021). Carbonyl Iron Powders as Absorption Material for Microwave Interference Shielding: A Review. *J. Alloys Compd.* 853, 157251. doi:10.1016/j.jallcom.2020.157251

Song, P., Liu, B., Liang, C., Ruan, K., Qiu, H., Ma, Z., et al. (2021). Lightweight, Flexible Cellulose-Derived Carbon Aerogel@Reduced Graphene Oxide/PDMS Composites with Outstanding EMI Shielding Performances and Excellent Thermal Conductivities. *Nano-Micro Lett.* 13, 1–17. doi:10.1007/s40820-021-00624-4

Vinayasree, S., Soloman, M., Sunny, V., Mohanan, P., Kurian, P., and Anantharaman, M. (2013). A Microwave Absorber Based on Strontium Ferrite-Carbon Black-Nitrile Rubber for S and X-Band Applications. *Compos. Sci. Technol.* 82, 69–75. doi:10.1016/j.compscitech.2013.04.010

Wang, D.-J., Zhang, J.-Y., He, P., and Hou, Z.-L. (2019). Size-modulated Electromagnetic Properties and Highly Efficient Microwave Absorption of Magnetic Iron Oxide Ceramic Opened-Hollow Microspheres. *Ceram. Int.* 45, 23043–23049. doi:10.1016/j.ceramint.2019.07.352

Wang, J., Jia, Z., Liu, X., Dou, J., Xu, B., Wang, B., et al. (2021). Construction of 1D Heterostructure NiCo@C/ZnO Nanorod with Enhanced Microwave Absorption. *Nano-Micro Lett.* 13, 1–16. doi:10.1007/s40820-021-00704-5

Wang, L., Yu, X., Li, X., Zhang, J., Wang, M., and Che, R. (2020). MOF-derived Yolk-Shell Ni@C@ZnO Schottky Contact Structure for Enhanced Microwave Absorption. *Chem. Eng. J.* 383, 123099. doi:10.1016/j.cej.2019.123099

Wang, X.-X., Ma, T., Shu, J.-C., and Cao, M.-S. (2018). Confinedly Tailoring Fe3O4 Clusters-NG to Tune Electromagnetic Parameters and Microwave Absorption with Broadened Bandwidth. *Chem. Eng. J.* 332, 321–330. doi:10.1016/j.cej.2017.09.101

Weng, L., Lei, X., Liu, J., Hu, H., Wang, J., and Zhang, Z. (2022). Three-dimensional Network FeNi/C Composites with Excellent Microwave-Absorbing Properties. *J. Alloys Compd.* 906, 164301. doi:10.1016/j.jallcom.2022.164301

Xu, W., Pan, Y.-F., Wei, W., Wang, G.-S., and Qu, P. (2018). Microwave Absorption Enhancement and Dual-Nonlinear Magnetic Resonance of Ultra Small Nickel with Quasi-One-Dimensional Nanostructure. *Appl. Surf. Sci.* 428, 54–60. doi:10.1016/j.apsusc.2017.09.052

Xu, Y., Yan, Z., and Zhang, D. (2015). Microwave Absorbing Property of a Hybrid Absorbent with Carbonyl Irons Coating on the Graphite. *Appl. Surf. Sci.* 356, 1032–1038. doi:10.1016/j.apsusc.2015.08.162

Yang, M., Yuan, Y., Li, Y., Sun, X., Wang, S., Liang, L., et al. (2020). Dramatically Enhanced Electromagnetic Wave Absorption of Hierarchical CNT/Co/C Fiber Derived from Cotton and Metal-Organic-Framework. *Carbon* 161, 517–527. doi:10.1016/j.carbon.2020.01.073

Zhang, K.-L., Zhang, J.-Y., Hou, Z.-L., Bi, S., and Zhao, Q.-L. (2019). Multifunctional Broadband Microwave Absorption of Flexible Graphene Composites. *Carbon* 141, 608–617. doi:10.1016/j.carbon.2018.10.024

Zhao, H., Cheng, Y., Lv, H., Ji, G., and Du, Y. (2019). A Novel Hierarchically Porous Magnetic Carbon Derived from Biomass for Strong Lightweight Microwave Absorption. *Carbon* 142, 245–253. doi:10.1016/j.carbon.2018.10.027

Zhou, C., Wu, C., Liu, D., and Yan, M. (2019). Metal-Organic Framework Derived Hierarchical Co/C@V2 O3 Hollow Spheres as a Thin, Lightweight, and High-Efficiency Electromagnetic Wave Absorber. *Chem. Eur. J.* 25, 2234–2241. doi:10.1002/chem.201805565